

# Strongly Coupled Photonic Moiré Superlattices

Chang-Hwan Yi,<sup>1,\*</sup> Hee Chul Park,<sup>1,†</sup> and Moon Jip Park<sup>1,‡</sup>

<sup>1</sup>Center for Theoretical Physics of Complex Systems,  
Institute for Basic Science (IBS), Daejeon, 34126, Republic of Korea

(Dated: September 1, 2021)

The moiré superlattice of misaligned atomic bilayers paves the way for designing a new class of materials with wide tunability. In this work, we propose a photonic analog of the moiré superlattice based on dielectric resonator quasi-atoms. In sharp contrast to van der Waals materials with weak interlayer coupling, we realize the strong coupling regime in a moiré superlattice, characterized by cascades of robust flat bands at large twist angles. Surprisingly, we find that these flat bands are characterized by a non-trivial band topology, the origin of which is the moiré pattern of the resonator arrangement. The physical manifestation of the flat band topology is a robust one-dimensional conducting channel on the edge, protected by the reflection symmetry of the moiré superlattice. By explicitly breaking the underlying reflection symmetry on the boundary terminations, we show that the first-order topological edge modes naturally deform into higher-order topological corner modes. Our work pioneers the physics of the moiré superlattice beyond the weakly coupled regime and introduces a designable platform to control photonic topological insulator phases using moiré patterns.

## INTRODUCTION

When two sheets of atomic bilayers are stacked with a finite rotation angle, the periodicity of the two incommensurate layers produces a large moiré superlattice. This giant amplification of the crystalline periodicity is the hallmark of moiré materials [1] and provides a viable platform for band structure engineering. Magic-angle twisted bilayer graphene is the representative example, exhibiting a variety of novel quantum phases such as superconductivity [2], correlated insulators [3–5], and topological phases [6–8]. At the microscopic level, van der Waals coupling between the two layers is a weak interaction, but it is the key ingredient that drives the drastic deformation of the band structure [9].

A photonic resonator array provides an attractive platform to explore the physics of moiré materials. Realizing a moiré superlattice in photonic crystals has clear advantages over electronic systems as the interactions in photonic crystals are not limited to weak van der Waals coupling. The tunable geometry and dielectricity of the photonic crystals allow a feasible control of the interlayer couplings [10]. Indeed, photonic systems can expand the scope of moiré materials beyond the weak coupling

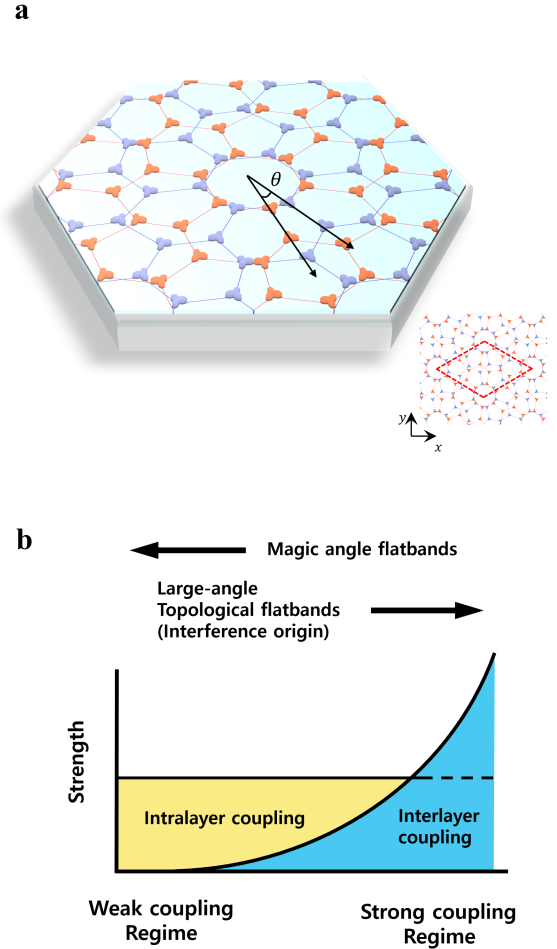


FIG. 1. **a.** Picture of the photonic moiré superlattice. Two honeycomb lattices of dielectric resonator quasi-atoms (red and blue) are overlaid with twist angle  $\theta$ . The primitive unit cell in the right panel is marked with the red rhombus and contains 28 quasi-atoms. **b.** Schematic illustration of the strong coupling regime of the moiré superlattice. As the interlayer couplings exceed the intralayer couplings, we find topological flat bands at large twist angles. This feature is in direct contrast with the weak coupling regime, where flat bands appear only at the magic angles.

regime.

In this work, we propose to apply a photonic lattice of resonators to explore the strong coupling regime of moiré materials. Although the photonic moiré superlattice has a direct analogy with twisted bilayer graphene [11–13], we

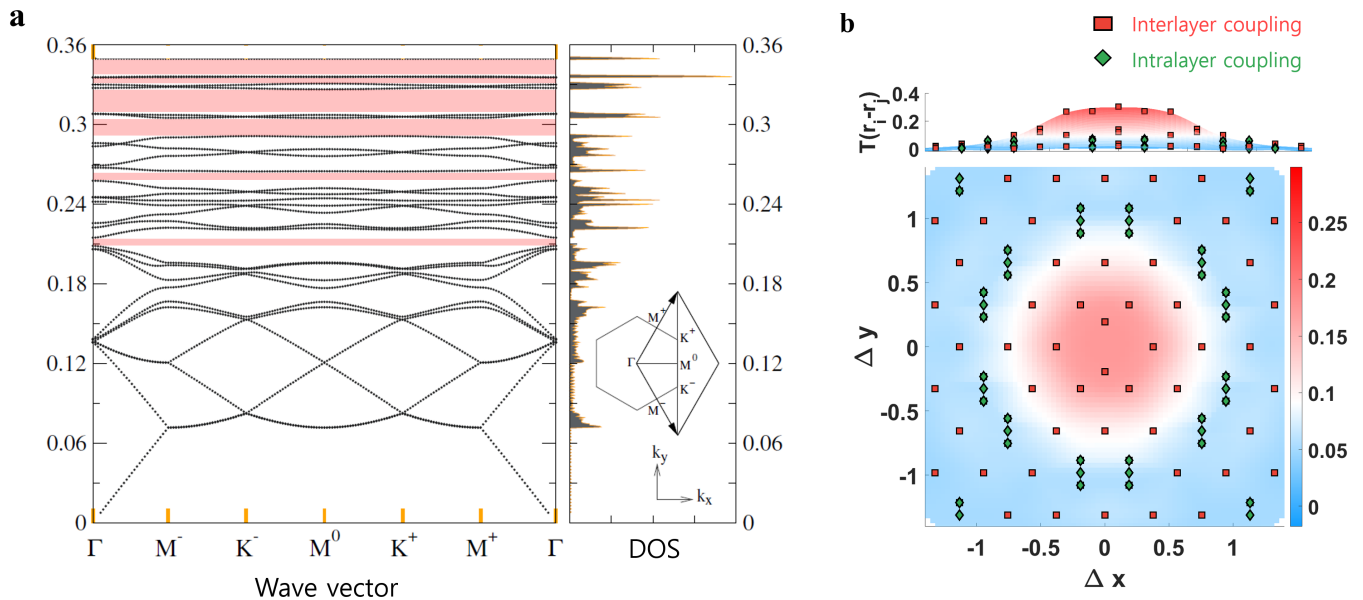


FIG. 2. **a.** Band structure of the lowest 28 photonic energy bands. Contrary to the weak coupling regime of the moiré superlattice, we find large gap openings in the high energy modes (pink regions). **b.** Hopping strength as a function of the displacement between two different quasi-atoms along the  $x$  and  $y$  directions. We find that the strength of the interlayer coupling (red squares) dominates over the intralayer coupling (green diamonds). This result directly verifies that our photonic crystal exhibits the strong coupling regime of the moiré superlattice.

find a drastically different band structure distinct from the standard phenomenology of its electronic counterpart. For the first time, we discover the emergence of robust flat bands at arbitrary large twist angles. These flat bands have particular localization patterns that are unique to the large-angle moiré superlattice. Furthermore, the flat bands are characterized by a non-trivial topological invariant that is protected by reflection symmetry. Physical manifestations include one-dimensional helical edge modes and higher-order topological corner modes. Our work provides a novel platform to design photonic topological materials and topological waveguides [14, 15] utilizing the moiré superlattice.

## RESULTS

**Photonic moiré superlattice** – Our photonic moiré superlattice is constructed by twisting two honeycomb photonic crystals with AA stacking around the hexagonal center. Figure 1a exemplifies our system setup with a rotation angle of  $\theta = 21.78^\circ$ , which forms the smallest possible moiré superlattice [16, 17]. Each photonic crystal site consists of a quasi-atom established upon a dielectric resonator [18, 19]. A set of 28 quasi-atoms forms a single moiré unit cell, as shown in the right panel of Fig. 1a. To obtain the energy bands of the optical modes, we solve the two-dimensional Helmholtz wave equation,

$$-\nabla^2 \psi = n^2(\mathbf{r}) \frac{\omega^2}{c^2} \psi, \quad (1)$$

imposing proper periodic boundary conditions. Here,

$n(\mathbf{r})$  is the piecewise constant refractive index, and  $\omega = ck$  is the free-space temporal frequency with a vacuum wavenumber  $k$ . In a single circular-shaped dielectric resonator, the resonator mode comprises multiple quasi-atomic orbitals with different azimuthal orbital numbers,  $l$ , such that  $\Psi(r, \theta) \sim \psi(r) \exp(i l \theta)$  [20, 21].

Given the moiré superlattice of optical resonators, we find that a number of energy bands stemming from different azimuthal orbital number sectors severely overlap one another in the low  $n$  regime (e.g.,  $n \sim 2$ , etc.). This is due to the weak confinement inside the resonators that enhances the resonator-resonator mode couplings. Contrarily, as  $n$  increases (up to 4 in our case), these couplings are suppressed to the tunneling regime, where the whole band structure is energetically separated into a set of 28 distinct bands (equivalent to the number of quasi-atoms in a single unit cell). In Fig. 2a, we show those of the lowest 28 bands corresponding to linear combinations of the single quasi-atomic modes with  $l = 0$  (see the Supplementary Material for the detailed wave characters of each band). The following sequential bundles of 28 bands are from combinations of the single atomic modes with  $l \geq 1$ .

As the bands with  $l = 0$  and  $l \geq 1$  are energetically decoupled in this high refractive index regime, the localized Wannier orbitals can be reconstructed from the solution of the Helmholtz equation. The effective tight-binding model that exactly reproduces the energy dispersion of

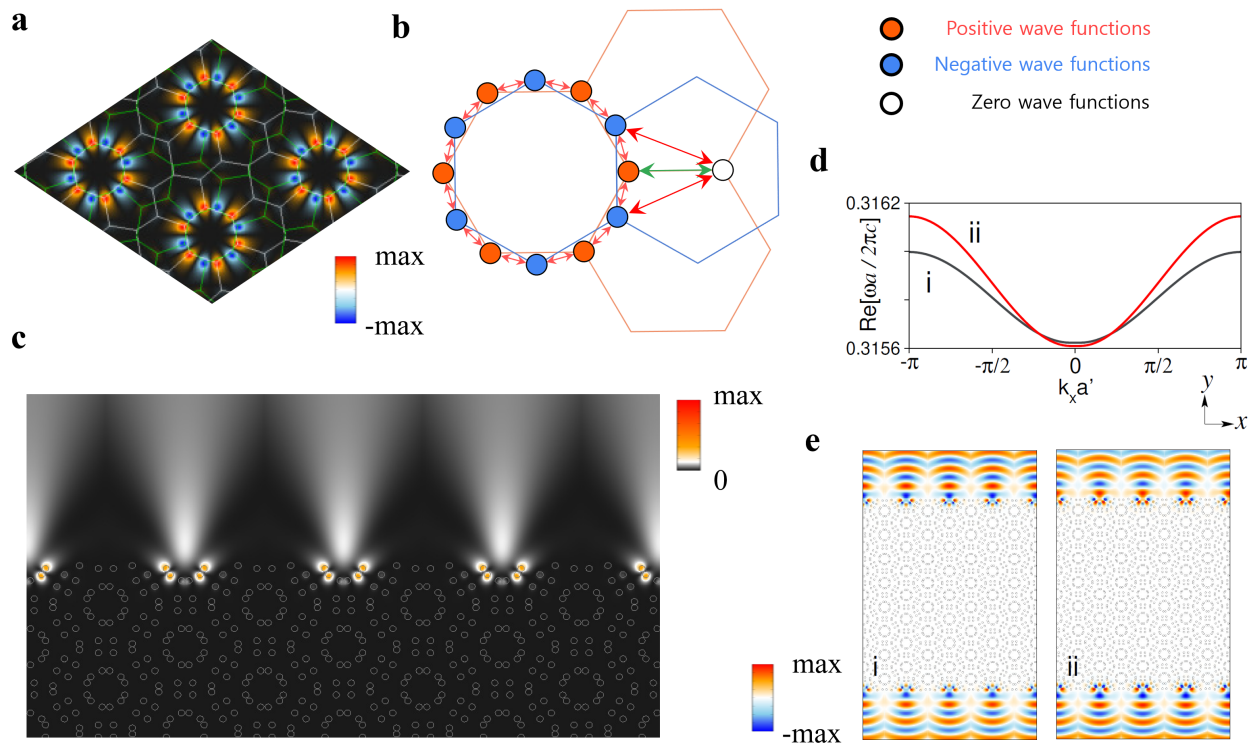


FIG. 3. **a.** Wave function of the flat bands. We find that the wave functions form localized standing waves around the innermost dodecagonal quasi-atoms near the rotational center with sign oscillations. **b.** Illustration of the destructive interference effect in the wave functions of the flat bands. The alternating signs of the standing waves introduce destructive interference in the hopping to outer quasi-atoms. **c.** Intensity ( $|\psi|^2$ ) pattern of the edge modes magnified along the upper edge of the lattice. **d.** and **e.** Energy dispersion of two edge modes and corresponding wave functions. Wave functions i and ii represent the symmetric and antisymmetric modes, respectively.

the photonic bands can be obtained as

$$H = \sum_{i,j} T(\mathbf{r}_i - \mathbf{r}_j) |\mathbf{r}_i\rangle \langle \mathbf{r}_j| + \text{h.c.}, \quad (2)$$

where  $|\mathbf{r}_i\rangle$  is the  $i$ -th localized quasi-atomic state at site  $\mathbf{r}_i$ , and  $T(\mathbf{r}_i - \mathbf{r}_j)$  is the effective hopping strength between sites  $i$  and  $j$  (see the Supplementary Material for the detailed algorithm of the Wannierization). Figure 2b shows  $T(\mathbf{r}_i - \mathbf{r}_j)$  as a function of the spatial displacement between two quasi-atoms, where the red squares and green diamonds represent the coupling between interlayer and intralayer sites, respectively. We find that the strength of the interlayer coupling dominates over that of the intralayer coupling. As a result, our analysis directly verifies the strongly coupled regime of the moiré superlattice.

**Flat bands in the strongly coupled regime** – We focus on the set of the bands with  $l = 0$ . First of all, in the low-energy bands, robust gap closings are observed at the  $K^+$  and  $K^-$  points in the Brillouin zone (BZ). Such gap closings are reminiscent of the Dirac cones that have been previously observed in monolayer honeycomb lattices and are protected by  $\pi$  Berry phases. We additionally dis-

cover large gap openings (pink bands in Fig. 2a) separating multiple flat bands at higher energies ( $\omega a / 2\pi c \gtrsim 0.2$ ). The large gap openings are a distinct feature compared to the gapless spectrum of a single-layer honeycomb lattice (see the Supplementary Material). Furthermore, we find that the wave characters of the emergent flat bands form anomalously localized states within the innermost dodecagonal quasi-atoms near the rotation center (see Fig. 3a).

The localized wave functions of the flat bands can be represented as standing waves with sign oscillations:

$$\Psi \sim \sum_{\alpha} (-1)^{\alpha} \psi_{\alpha}, \quad (3)$$

where  $\psi_{\alpha}$  is the localized wave function in the innermost dodecagonal quasi-atoms with  $\alpha \in \{1, 2, 3, \dots, 12\}$ . The couplings marked by red colors in Fig. 2b represent the dominant couplings between the innermost dodecagonal quasi-atoms. Although we still find finite couplings to other sites, the standing waves cannot propagate further to the outer quasi-atomic sites, as the sign change in the wave functions produces destructive interference to the outer sites (red and green arrows in Fig. 3b). As a result, the wave functions of the innermost quasi-atoms form a

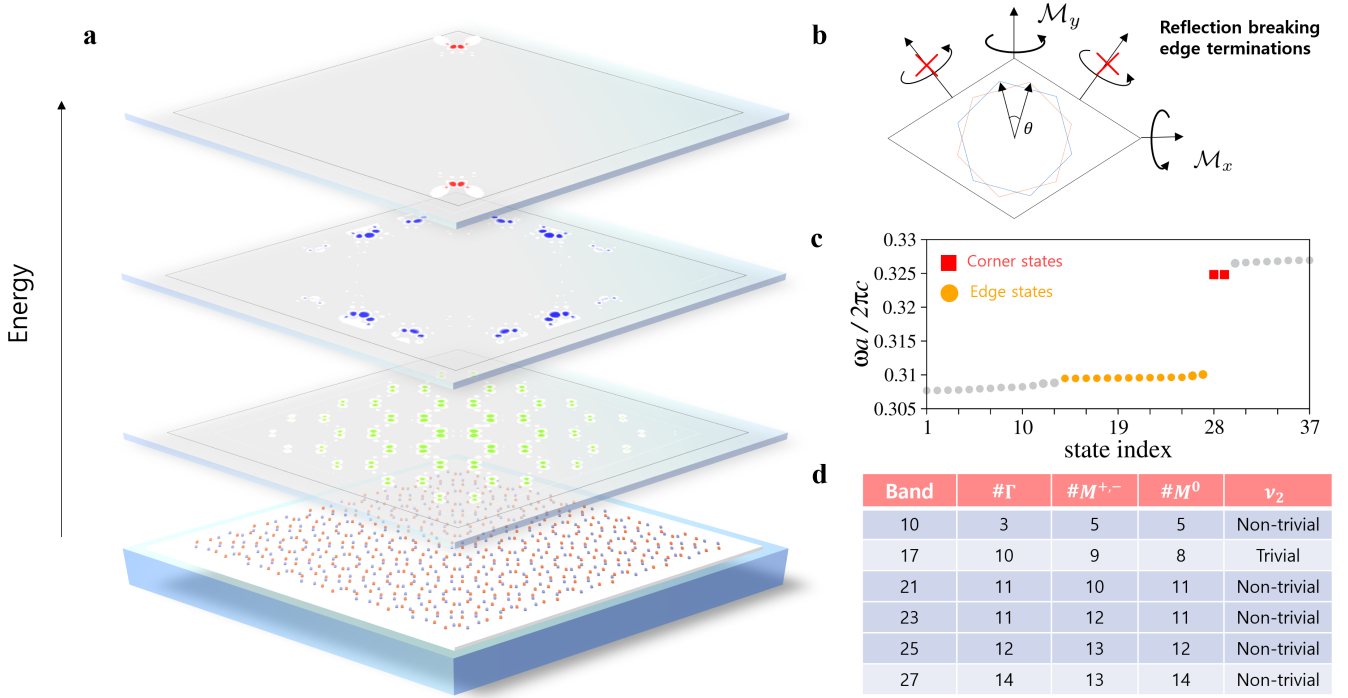


FIG. 4. **a.** Eigenstates of the bulk (green), edge (blue), and corner (red) states in a finite-size moiré superlattice ( $5 \times 5$  primitive unit cell). **b** Schematic illustrations of different edge terminations. In the reflection symmetric terminations, we find the one-dimensional edge modes. In generic terminations that break the reflection symmetry, we can still define the inversion symmetric higher-order topological phase, which manifests as the topological corner modes. **c.** Energy eigenvalues in the finite size systems. Red square and yellow circle represent the corner and edge states respectively. Gray dots represent the bulk states. **d.** Table representing the symmetry classifications of the wave functions and the second Stiefel-Whitney number of each band gap. The second Stiefel-Whitney number is determined by the number of occupied inversion-odd bands at the TRIM points.

localized standing wave with flat bands. The destructive interference is universally observed at arbitrary large angles, and it is strongly enhanced in the limit  $\theta \rightarrow 30^\circ$ . This particular type of localization is only possible if the strengths of the interlayer and intralayer hoppings are comparable, and it serves as the hallmark of the strong coupling regime of the moiré superlattice.

**Non-trivial topology induced by a moiré pattern** – Despite the complicated quasi-atom configurations, the moiré superlattice in this work possesses reflection symmetries  $\mathcal{M}_x$  and  $\mathcal{M}_y$  along the  $\hat{x}$ - and  $\hat{y}$ -axis (see Fig. 4b). These symmetries are preserved regardless of the twist angle and allow us to classify the Bloch wave functions at the time-reversal invariant moment ( $\mathbf{k} \in \{\Gamma, M^0, M^+, M^-\}$ ) into four distinct symmetry sectors depending on the relative phase between the four Cartesian quadrants:

$$\begin{aligned}
 \text{I} & : \Psi(x, y) = \Psi(-x, y) = \Psi(x, -y), \\
 \text{II} & : \Psi(x, y) = -\Psi(-x, y) = \Psi(x, -y), \\
 \text{III} & : \Psi(x, y) = \Psi(-x, y) = -\Psi(x, -y), \\
 \text{IV} & : \Psi(x, y) = -\Psi(-x, y) = -\Psi(x, -y).
 \end{aligned} \quad (4)$$

The symmetry classifications of the Bloch wave functions

further allow a finer topological classification characterized by reflection-symmetry-protected polarization. As the system can be decomposed into even and odd  $\mathcal{M}_x$  sectors ( $+ \in \{\text{I, II}\}$ ,  $- \in \{\text{III, IV}\}$ ), we can separately define the bulk polarization of each sector as

$$\nu_{\pm} = i \oint d\mathbf{k} \mathcal{A}(\mathbf{k})_{\pm}, \quad (5)$$

where cyclic integration is performed along the reflection symmetric line  $\Gamma - M - \Gamma$ .  $\mathcal{A}(\mathbf{k})_{\pm} = \langle \Psi_{\pm} | \partial_{\mathbf{k}} | \Psi_{\pm} \rangle$  is the Berry connection defined for each reflection sector. The additional reflection symmetry,  $\mathcal{M}_y$ , further ensures  $\mathbb{Z}_2$  classification of the bulk polarizations,  $\nu_{\pm} \in \{0, \pi\}$ . Evaluating the polarization for each band gap, we find that the multiple band gaps separating the flat bands possess non-trivial polarization,  $\nu \equiv \nu_+ = \nu_- = \pi$ , while the overall polarization,  $\nu \equiv \nu_+ + \nu_- = 0$ , is always trivial (see the Supplementary Material for the detailed calculation). The non-trivial polarization with  $\nu_{\pm} = \pi$  manifests as one-dimensional topological boundary modes. To explicitly show this feature, we consider a slab geometry with open boundary conditions along the  $\hat{y}$ -direction. Figure 3d shows that a pair edge spectrum emerges within the gapped region in the bulk bands. The two

modes correspond to symmetric and antisymmetric edge modes localized on each side of the boundary (see Fig. 3e).

**Higher-order topology without reflection symmetry** – The topological edge modes are robust against any arbitrary perturbations, preserving the underlying reflection symmetries. However, boundary terminations along an arbitrary direction naturally break the reflection symmetries. In such a case, the polarization,  $\nu$ , is ill-defined, and the topological robustness of the edge modes becomes deficient. Nevertheless, the product of the two reflection symmetries, which acts as an inversion,  $\mathcal{P} = \mathcal{M}_x \times \mathcal{M}_y$ , can be preserved. Such novel orientational dependence of the moiré pattern realizes a richer topological structure, characterized by the second Stiefel–Whitney number,  $\nu_2$ . We assign  $\nu_2$  using the parity eigenvalues of the occupied bands at time-reversal invariant momenta (TRIM)  $\Gamma_i \in \{\Gamma, M^0, M^+, M^-\}$  as

$$(-1)^{\nu_2} = \prod_{\Gamma_i \in \text{TRIM}} (-1)^{[N_{\text{occ}}^-(\Gamma_i)/2]}, \quad (6)$$

where  $N_{\text{occ}}^-(\Gamma_i)$  is the number of bands below the band gap that belong to symmetry sectors II and III at  $\Gamma_i$  [22]. In our specific case, we count the number of bands corresponding to symmetry sectors II and III. Figure 4d shows the resulting symmetry classifications of each band gap, where several band gaps separating the flat bands are characterized by the non-trivial  $\nu_2$ . The non-trivial second Stiefel–Whitney number manifests as topological corner modes in a finite-size flake geometry with an open boundary (Red states in Fig. 4a). We indeed find the mid-gap topological corner modes to be strongly localized at the inversion symmetric corners, in addition to being reminiscent of the one-dimensional edge modes (Blue states in Fig. 4a). These topological corner modes remain robust against arbitrary perturbations as long as the inversion symmetry is intact.

## DISCUSSION

This work firstly demonstrates the strong interlayer coupling regime of a moiré superlattice of photonic crystals. Silicon (Si)-based materials have a typical refractive index of  $3.5 < n < 7$  for a wavelength of  $0.35 \mu\text{m} < \lambda < 2 \mu\text{m}$ , while that of semiconductor alloys such as GaAs, AlGaSb, and InGaAsP is  $3.3 < n < 5$  for a wavelength of  $0.35 \mu\text{m} < \lambda < 2 \mu\text{m}$  [23, 24]. Our demonstration can be experimentally realized in these materials.

We also newly discover the emergence of topological flat bands at large twist angles. This feature, which has not been observed in electronic systems, is the hallmark of our photonic moiré superlattice. The non-trivial topology of the moiré pattern realizes a tunable deformation of the one-dimensional edge modes and topological corner modes. Our topological material design using a moiré superlattice can be a promising start in the hunt for engineering a variety of topological photonic phases and for practical photonic device applications.

## METHODS

The energy bands of the optical modes in the photonic crystals are obtained by solving the Maxwell equations reduced to the Helmholtz wave equation,

$$-\nabla^2 \psi = n^2(\mathbf{r}) \frac{\omega^2}{c^2} \psi, \quad (7)$$

where  $n(\mathbf{r})$  is the piecewise constant refractive index, and  $\omega = ck$  is the free-space temporal frequency with vacuum wavenumber  $k$  and speed of light  $c$ . An individual quasi-atom has a refractive index of  $n = 4$  and a radius of  $r = a/6$  with a tunable  $C_3$  rotation symmetric deformation, where  $a$  is the original hexagonal lattice constant. Our results focus on the transverse-magnetic [ $TM$ ;  $\psi = (0, 0, E_z)$ ] polarization of the modes, while Eq. (7) governs the transverse-electric [ $TE$ ;  $\psi = (0, 0, H_z)$ ] mode as well. To avoid an overflow of the domain mesh in resolving our complicated bilayer structure that would lead to poor computational performance [25], we employ the boundary element method [26, 27] to tackle the numerical computations of Eq. (7). We calculate  $\omega/c$  in the two-dimensional lattice, the finite-size system, and the one-dimensional lattice by imposing, respectively, a two-dimensional periodic condition, a pure outgoing condition at infinity, and a mixed boundary condition. On top of the basic formalism of the boundary element method, we implement the block Sakurai–Sugiura method [28–32] to compute the photonic band structures. Details of the numerical methods and the boundary conditions can be found in the Supplementary Material.

## ACKNOWLEDGMENTS

We acknowledge financial support from the Institute for Basic Science in the Republic of Korea through the project IBS-R024-D1.

- 
- \* [yichanghwan@hanmail.net](mailto:yichanghwan@hanmail.net)  
† [hcpark@ibs.re.kr](mailto:hcpark@ibs.re.kr)  
‡ [moonjippark@ibs.re.kr](mailto:moonjippark@ibs.re.kr)
- [1] E. Y. Andrei and A. H. MacDonald, Graphene bilayers with a twist, *Nature Materials* **19**, 1265 (2020).
  - [2] Y. Cao, V. Fatemi, S. Fang, K. Watanabe, T. Taniguchi, E. Kaxiras, and P. Jarillo-Herrero, Unconventional superconductivity in magic-angle graphene superlattices, *Nature* **556**, 43 (2018).
  - [3] Y. Cao, V. Fatemi, A. Demir, S. Fang, S. L. Tomarken, J. Y. Luo, J. D. Sanchez-Yamagishi, K. Watanabe, T. Taniguchi, E. Kaxiras, R. C. Ashoori, and P. Jarillo-Herrero, Correlated insulator behaviour at half-filling in magic-angle graphene superlattices, *Nature* **556**, 80 (2018).
  - [4] X. Lu, P. Stepanov, W. Yang, M. Xie, M. A. Aamir, I. Das, C. Urgell, K. Watanabe, T. Taniguchi, G. Zhang, A. Bachtold, A. H. MacDonald, and D. K. Efetov, Superconductors, orbital magnets and correlated states in magic-angle bilayer graphene, *Nature* **574**, 653 (2019).
  - [5] A. Kerelsky, L. J. McGilly, D. M. Kennes, L. Xian, M. Yankowitz, S. Chen, K. Watanabe, T. Taniguchi, J. Hone, C. Dean, A. Rubio, and A. N. Pasupathy, Maximized electron interactions at the magic angle in twisted bilayer graphene, *Nature* **572**, 95 (2019).
  - [6] Z. Song, Z. Wang, W. Shi, G. Li, C. Fang, and B. A. Bernevig, All magic angles in twisted bilayer graphene are topological, *Phys. Rev. Lett.* **123**, 036401 (2019).
  - [7] M. J. Park, Y. Kim, G. Y. Cho, and S. Lee, Higher-order topological insulator in twisted bilayer graphene, *Phys. Rev. Lett.* **123**, 216803 (2019).
  - [8] B. Liu, L. Xian, H. Mu, G. Zhao, Z. Liu, A. Rubio, and Z. F. Wang, Higher-order band topology in twisted moiré superlattice, *Phys. Rev. Lett.* **126**, 066401 (2021).
  - [9] R. Bistritzer and A. H. MacDonald, Moiré bands in twisted double-layer graphene, *Proceedings of the National Academy of Sciences* **108**, 12233 (2011), <https://www.pnas.org/content/108/30/12233.full.pdf>.
  - [10] T. Ozawa, H. M. Price, A. Amo, N. Goldman, M. Hafezi, L. Lu, M. C. Rechtsman, D. Schuster, J. Simon, O. Zeitlinger, and I. Carusotto, Topological photonics, *Rev. Mod. Phys.* **91**, 015006 (2019).
  - [11] B. Lou, N. Zhao, M. Minkov, C. Guo, M. Orenstein, and S. Fan, Theory for twisted bilayer photonic crystal slabs, *Phys. Rev. Lett.* **126**, 136101 (2021).
  - [12] K. Dong, T. Zhang, J. Li, Q. Wang, F. Yang, Y. Rho, D. Wang, C. P. Grigoropoulos, J. Wu, and J. Yao, Flat bands in magic-angle bilayer photonic crystals at small twists, *Phys. Rev. Lett.* **126**, 223601 (2021).
  - [13] P. Wang, Y. Zheng, X. Chen, C. Huang, Y. V. Kartashov, L. Torner, V. V. Konotop, and F. Ye, Localization and delocalization of light in photonic moiré lattices, *Nature* **577**, 42 (2020).
  - [14] H. Deng, G. L. Lippi, J. Mørk, J. Wiersig, and S. Reitzenstein, Physics and applications of high- $\beta$  micro- and nanolasers, *Advanced Optical Materials*, 2100415 (2021).
  - [15] M. Parto, Y. G. N. Liu, B. Bahari, M. Khajavikhan, and D. N. Christodoulides, Non-hermitian and topological photonics: optics at an exceptional point, *Nanophotonics* **10**, 403 (2021).
  - [16] J. M. B. Lopes dos Santos, N. M. R. Peres, and A. H. Castro Neto, Graphene bilayer with a twist: Electronic structure, *Phys. Rev. Lett.* **99**, 256802 (2007).
  - [17] L. Zou, H. C. Po, A. Vishwanath, and T. Senthil, Band structure of twisted bilayer graphene: Emergent symmetries, commensurate approximants, and wannier obstructions, *Phys. Rev. B* **98**, 085435 (2018).
  - [18] H. Cao and J. Wiersig, Dielectric microcavities: Model systems for wave chaos and non-hermitian physics, *Rev. Mod. Phys.* **87**, 61 (2015).
  - [19] K. J. Vahala, Optical microcavities, *Nature* **424**, 839 (2003).
  - [20] K. J. Vahala, *Optical Microcavities* (WORLD SCIENTIFIC, 2004).
  - [21] R. K. Chang and A. J. Campillo, *Optical processes in microcavities*, Vol. 3 (World scientific, 1996).
  - [22] J. Ahn, S. Park, D. Kim, Y. Kim, and B.-J. Yang, Stiefel–whitney classes and topological phases in band theory, *Chinese Physics B* **28**, 117101 (2019).
  - [23] M. N. Polyanskiy, Refractive index database, <https://refractiveindex.info>.
  - [24] E. D. Palik, *Handbook of optical constants of solids*, Vol. 3 (Academic press, 1998).
  - [25] J. R. de Lasson, L. H. Frandsen, P. Gutsche, S. Burger, O. S. Kim, O. Breinbjerg, A. Ivinskaya, F. Wang, O. Sigmond, T. Häyrynen, A. V. Lavrinenko, J. Mørk, and N. Gregersen, Benchmarking five numerical simulation techniques for computing resonance wavelengths and quality factors in photonic crystal membrane line defect cavities, *Opt. Express* **26**, 11366 (2018).
  - [26] J. Wiersig, Boundary element method for resonances in dielectric microcavities, *Journal of Optics A: Pure and Applied Optics* **5**, 53 (2002).
  - [27] P. A. Knipp and T. L. Reinecke, Boundary-element method for the calculation of electronic states in semiconductor nanostructures, *Phys. Rev. B* **54**, 1880 (1996).
  - [28] J. Asakura, T. Sakurai, H. Tadano, T. Ikegami, and K. Kimura, A numerical method for nonlinear eigenvalue problems using contour integrals, *SIAM Letters* **1**, 52 (2009).
  - [29] H. Isakari, T. Takahashi, and T. Matsumoto, Periodic band structure calculation by the sakurai–sugiura method with a fast direct solver for the boundary element method with the fast multipole representation, *Engineering Analysis with Boundary Elements* **68**, 42 (2016).
  - [30] C.-J. Zheng, H.-F. Gao, L. Du, H.-B. Chen, and C. Zhang, An accurate and efficient acoustic eigensolver based on a fast multipole bem and a contour integral method, *Journal of Computational Physics* **305**, 677 (2016).
  - [31] T. Sakurai, Y. Futamura, and H. Tadano, Efficient parameter estimation and implementation of a contour integral-based eigensolver, *Journal of Algorithms & Computational Technology* **7**, 249 (2013), <https://doi.org/10.1260/1748-3018.7.3.249>.
  - [32] H. Gao, T. Matsumoto, T. Takahashi, and H. Isakari, Eigenvalue analysis for acoustic problem in 3d by boundary element method with the block sakurai–sugiura method, *Engineering Analysis with Boundary Elements* **37**, 914 (2013).
  - [33] G. Veble, T. Prosen, and M. Robnik, Expanded boundary integral method and chaotic time-reversal doublets in quantum billiards, *New Journal of Physics* **9**, 15 (2007).

- [34] R. Dubertrand, E. Bogomolny, N. Djellali, M. Lebental, and C. Schmit, Circular dielectric cavity and its deformations, *Phys. Rev. A* **77**, 013804 (2008).
- [35] J. Kullig and J. Wiersig, Perturbation theory for asymmetric deformed microdisk cavities, *Phys. Rev. A* **94**, 043850 (2016).
- [36] C.-L. Zou, H. G. L. Schwefel, F.-W. Sun, Z.-F. Han, and G.-C. Guo, Quick root searching method for resonances of dielectric optical microcavities with the boundary element method, *Opt. Express* **19**, 15669 (2011).

SUPPLEMENTARY MATERIAL FOR “STRONGLY COUPLED MOIRÉ PHOTONIC SUPERLATTICES”

Construction of the effective tight-binding model

To construct the effective tight-binding model, we extract the band energy and the wave functions at the time-reversal invariant momenta ( $\mathbf{k}_{\text{TRIM}} \in \{\Gamma, M^+, M^-, M^0\}$ ) from the solution of the Helmholtz equation. Then, the Bloch Hamiltonian of the lowest 28 bands can be reconstructed as

$$H(\mathbf{k}_{\text{TRIM}}) = U(\mathbf{k}_{\text{TRIM}})D(\mathbf{k}_{\text{TRIM}})U(\mathbf{k}_{\text{TRIM}})^\dagger, \quad (\text{S1})$$

where  $D(\mathbf{k})$  is the diagonal matrix consisting of the energies of the lowest 28 bands, and  $U(\mathbf{k}_{\text{TRIM}})$  is the unitary matrix containing the wave functions. More specifically,  $U(\mathbf{k}_{\text{TRIM}})$  is  $28 \times 28$  where the element  $U_{ij}$  is given as

$$U_{ij} = \int_i dA \Psi_j, \quad (\text{S2})$$

where  $\Psi_j$  is the solution of the Helmholtz equation for the  $j$ -th band. Area integration is performed in the interior region of the  $i$ -th resonator.

After deriving the Bloch Hamiltonian at the TRIM points, we can reconstruct the real space tight-binding model. To do so, we notice that the Bloch Hamiltonian can be expressed by systems of the linear equations for the hopping matrices as follows:

$$\begin{aligned} H(\Gamma) &= H_{(0,0)} + H_{(1,0)} + H_{(-1,0)} + H_{(0,1)} + H_{(0,-1)} + H_{(1,1)} + H_{(-1,-1)} + H_{(1,-1)} + H_{(-1,1)}, \\ H(M^+) &= H_{(0,0)} - H_{(1,0)} - H_{(-1,0)} + H_{(0,1)} + H_{(0,-1)} - H_{(1,1)} - H_{(-1,-1)} - H_{(1,-1)} - H_{(-1,1)}, \\ H(M^-) &= H_{(0,0)} + H_{(1,0)} + H_{(-1,0)} - H_{(0,1)} - H_{(0,-1)} - H_{(1,1)} - H_{(-1,-1)} - H_{(1,-1)} - H_{(-1,1)}, \\ H(M^0) &= H_{(0,0)} - H_{(1,0)} - H_{(-1,0)} - H_{(0,1)} - H_{(0,-1)} + H_{(1,1)} + H_{(-1,-1)} + H_{(1,-1)} + H_{(-1,1)}, \end{aligned} \quad (\text{S3})$$

where  $H_{(m,n)}$  is the hopping matrix from a moiré unit cell to the neighbor unit cell translated by the vector  $\vec{L} = m\mathbf{b}_1 + n\mathbf{b}_2$ . Hence,  $H_{(0,0)}$  is the hopping matrix within the same unit cell. In addition to the above equations, the translational symmetry imposes the condition  $H_{(m,n)} = H_{(n,m)}^\dagger$ . With all these conditions, we are able to solve the above systems of the linear equations to derive the hopping strength between different sites. Figure S1 shows a comparison of the energy bands derived from the full Helmholtz equations and from the effective tight-binding model. We find the two results to agree quite well.

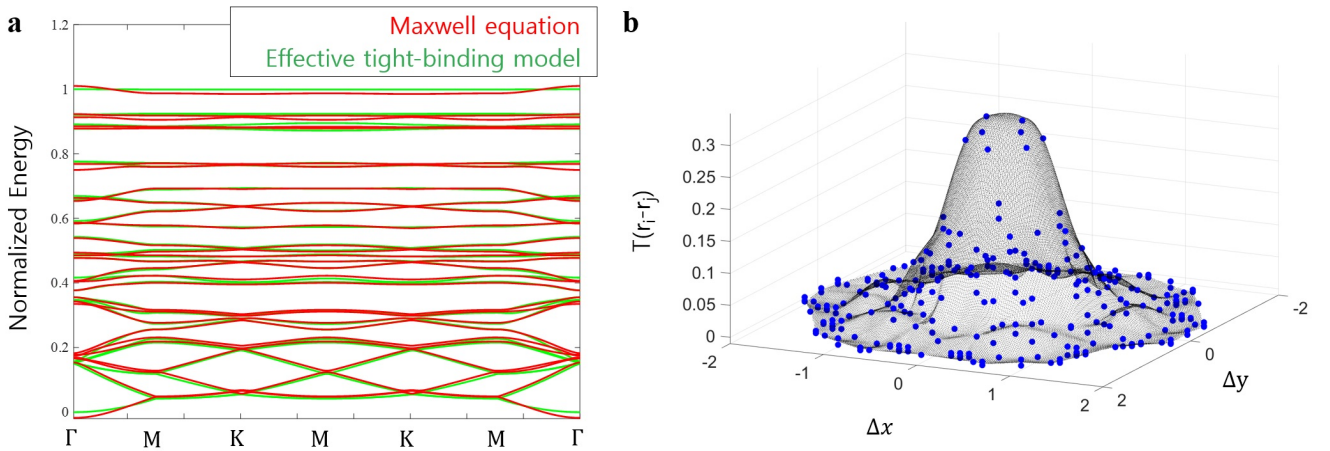


FIG. S1. **a.** Comparison of the band structures derived from the Maxwell equation (red) and the effective tight-binding model (green). **b.** Effective hopping strength as a function of the displacement between two quasi-atoms.

## Detailed calculation of the photonic band structure

To numerically compute the band structures of our two-dimensional photonic crystal, we utilize the so-called boundary element method (BEM) [26, 27], a discretized version of the boundary integral equation (BIE). The BEM is a powerful tool [25] for obtaining eigenstates (or quasi-normal modes or resonances) in piecewise homogeneous systems. This method does not require a full spatial domain mesh to calculate fields; it only needs to know the wavefunctions and their outward normal derivative on the domain boundaries of the involved subsystems. As the current state of BEM development is already in the textbook stage, we only briefly introduce a few of its core ideas here.

### Boundary element method

We can combine the free-space Green function  $G$  and unknown solution  $\psi$  given as solutions of the Helmholtz equations as

$$\left[ \nabla^2 + n^2 \frac{\omega^2}{c^2} \right] G\left(r, r'; \frac{\omega}{c}\right) = \delta(r - r') , \quad \left[ \nabla^2 + n^2 \frac{\omega^2}{c^2} \right] \psi\left(r; \frac{\omega}{c}\right) = 0 \quad (\text{S4})$$

for a domain enclosed by a simple-connected-closed envelope  $\Gamma$ . Here,  $(r, r')$  is inside  $\Gamma$ ,  $G(r, r'; \omega/c) = -i/4H_0^{(1)}(n\omega|r - r'|/c)$  in two dimensions, and  $\delta(r - r')$  is the two-dimensional Dirac delta function, where  $H_0^{(1)}$  is the first kind Hankel function of order 0. The two equations can be nested by subtracting one another after properly multiplying  $\psi$  and  $G$  to the two equations, as follows:

$$\psi\delta(r - r') = \psi\nabla^2 G - G\nabla^2\psi = \nabla[\psi\nabla G - G\nabla\psi]. \quad (\text{S5})$$

The two-dimensional 'area integration' inside  $\Gamma$  gives  $\psi$  on the LHS, while we can reduce this domain integral to the 'line integraion' along  $\Gamma$  on the RHS by applying Green's second identity. Then, it explicitly induces a boundary integral equation for unknown  $\psi(s)$ ,  $\partial_\nu\psi(s)$ , and  $\omega/c$ , as follows:

$$\psi(r') = \oint_\Gamma ds \left[ \psi(s)\partial_\nu G\left(s, r'; \frac{\omega}{c}\right) - G\left(s, r'; \frac{\omega}{c}\right) \partial_\nu\psi(s) \right]. \quad (\text{S6})$$

Here,  $r'$  is an arbitrary point inside  $\Gamma$  and  $s \in \Gamma$ , and  $\partial_\nu$  denotes the outward normal derivative. By pushing  $r'$  to be involved in  $\Gamma$  too, as  $r' \rightarrow s' \in \Gamma$ , we can complete the BIE formulation. Note that we can circumvent the singular point of  $G(s, s' = s)$  in terms of the Cauchy principal value.

By meshing  $\Gamma$  into  $N$  number of segments, the BIE turns into a  $2N \times 2N$  matrix equation of the BEM,

$$\left[ \int_{\gamma_i} G\left(s_i, s'_j; \frac{\omega}{c}\right) dl \quad \int_{\gamma_j} \partial_\nu G\left(s_i, s'_j; \frac{\omega}{c}\right) dl \right] \begin{bmatrix} \partial_\nu\psi(s'_j) & \psi(s'_j) \end{bmatrix}^T = 0, \quad (\text{S7})$$

where  $1 \leq i, j \in \mathbb{N} \leq N$ , and  $\gamma_j$  is the segment length of the  $j$ -th element having a center position at  $s'_j(x, y)$ . Having fixed the boundary shape of  $\Gamma$ , which is divided by a proper number of element  $N$ , the matrix equation

$$M_{i,j}(\omega/c) \Psi = 0 \quad (\text{S8})$$

produces, in principle, an infinite number of solutions for  $\omega/c$  and corresponding vectors  $\Psi$ . The nonlinear eigenvalue problem Eq. (S8) cannot be solved directly through a one-step diagonalization for  $\omega/c$ ; instead, we have to iteratively find solutions  $E$  starting from a proper initial guess  $E_0$ . It is known that this root-search strategy functions well and is robust with the aid of several efficient numerical methods, e.g., those in [33–36], provided that  $E_0$  is close enough to  $E$ . Nevertheless, preparing good quality initial guesses remains a challenging task, and more critically, this approach can be found to be insufficient when it comes to computing the complete structure of photonic energy bands.

With this motivation, we adopt a more systematic approach that operates with the 'contour integral' of matrix  $M$  for  $\omega/c \in \mathbb{C}$ . Among several variations of this approach, we implement a block version of the Sakurai–Sugiura method (block SS) following [28–32]. From a practical viewpoint, this method can provide numerous good quality initial guesses. The reason for using an additional refinement iterative process is because this method produces undesired solutions. Although it seems that the block SS method has yet to be well introduced in the optical BEM community, it is found in our work that this method is remarkably helpful to compute the eigenstates, particularly when we are to compute photonic band structures. We emphasize that the block SS method itself was originally designed to self-consistently give the exact solutions at once without extra iterative computations like we have done in our work. Below, forgoing the sophisticated mathematical proofs involved in this method, its essence is outlined.

*Block Sakurai–Sugiura contour integral method*

Given the constructed matrix  $M(\omega/c)$  for the BEM, we can define the moment matrix given as

$$\mu_j = \frac{1}{2\pi i} \oint_C z^j v^H M^{-1} v dz, \quad (\text{S9})$$

where  $z \leftarrow \omega/c \in \mathbb{C}$ ,  $v \in \mathbb{C}^{2N \times k}$ ,  $\{j, k\} \in \mathbb{N}$ , and the contour  $C$  is set to enclose the target solutions of  $\omega/c$ . Note that the entries in  $v$  are complex-valued random numbers. After obtaining  $\mu_j$ , we can construct two Hankel matrices:

$$H_m^R = \begin{pmatrix} \mu_0 & \mu_1 & \cdots & \mu_{m-1} \\ \mu_1 & \mu_2 & \cdots & \mu_m \\ \vdots & \vdots & \ddots & \vdots \\ \mu_{m-1} & \mu_m & \cdots & \mu_{2m-2} \end{pmatrix}, \quad H_m^L = \begin{pmatrix} \mu_1 & \mu_2 & \cdots & \mu_m \\ \mu_2 & \mu_3 & \cdots & \mu_{m+1} \\ \vdots & \vdots & \ddots & \vdots \\ \mu_m & \mu_{m+1} & \cdots & \mu_{2m-1} \end{pmatrix}. \quad (\text{S10})$$

According to the proofs in [28], the eigenvalues  $\lambda_l$  of the pencil

$$H_m^L = \lambda_l H_m^R, \quad (l = 1, \dots, m) \quad (\text{S11})$$

are the same ones in our original BEM up to  $m$ , as

$$M_{i,j}(\lambda_l = \omega_l/c)\Psi = 0. \quad (\text{S12})$$

Although we successfully transformed our original BEM into a one-step diagonalization problem, there are still some remaining challenges in this method. First, a good approximation of the contour integral in Eq. (S9); second, a proper choice of order  $j$  for the moment matrix  $\mu_j$ ; and third, a reliable column number  $k$  of vectors  $v$ . The first issue is concerned with the selection of the integral contour shape, with a numerical integration typically carried out through the conventional trapezoidal rule. In our work, we use an elliptical polygon path of the integral contour [30, 31], given as

$$\frac{\omega}{c} = \frac{\omega_0}{c} + \rho(\cos \theta_l + i\eta \sin \theta_l), \quad \theta_l = \frac{2\pi}{\mathcal{N}}(l + 1/2), \quad (\text{S13})$$

where  $\mathcal{N}$  is the number of segments for the integral contour  $C$ . Then, the integral in Eq. (S9) is numerically calculated by a discrete sum [30, 31], as

$$\mu_j \approx \frac{1}{\mathcal{N}} \sum_{l=0}^{\mathcal{N}-1} \rho \left[ \frac{\omega_l - \omega_0}{c\rho} \right]^l [\eta \cos \theta_l + i \sin \theta_l] v^H M^{-1} v. \quad (\text{S14})$$

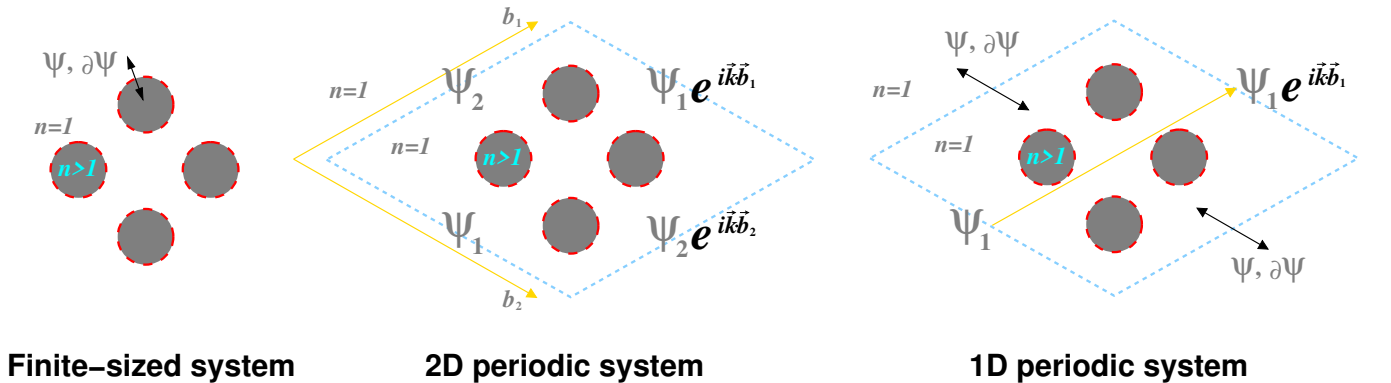


FIG. S2. Schematic illustrations of the resonator-vacuum boundary (red dashed) and the vacuum-vacuum (blue dashed) virtual boundary that are used for computing band structures through the BEM. The latter boundary defines the primitive unit cell with the translation vectors  $(\vec{b}_1, \vec{b}_2)$  for a two-dimensional periodic system and  $\vec{b}_1$  for a one-dimensional one. In all boundary cases, the wave functions  $\psi$  and its normal derivative  $\partial_\nu \psi$  are continuous.  $n$  and  $\vec{k}$  represent the refractive index and the Bloch wave vector, respectively.

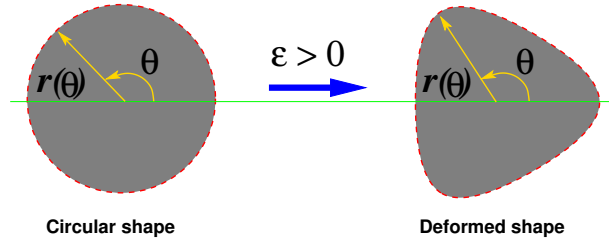


FIG. S3. Deformed single resonator quasi-atom whose boundary is defined by Eq. (S15) with  $(t, \theta_0) = (3, 0)$ .

Since the scale factor  $\eta$  controls the width of the elliptical shape in the imaginary value direction, if the value is small, the contour  $C$  can tightly enclose the real axis in the complex plane, while the elliptical shape becomes circular when  $\eta = 1$ . As the contour  $C$  is shifted by  $\omega_0/c$  and is scaled by  $\rho$ , our desired solution can be recovered after compensating this shift-scale over the obtained eigenvalue  $\lambda$ , as  $\omega/c = \omega_0/c + \rho\lambda$ .

#### *Periodic boundary conditions for 1D and 2D structures*

Generally, the BEM is employed to compute eigenstates in isolated sub-systems embedded in an infinite-extended environment (see the leftmost schematic in Fig. S2). These eigenstates satisfy the Sommerfeld pure outgoing condition, which is adequate in the finite-size systems that we have examined in the main text to exemplify the edge and corner modes. To obtain the photonic energy band structures, we impose a Bloch boundary condition on the pairwise virtual boundaries (according to the translation vectors of the unit cell) constructed in the environmental domain outside the resonators. The composite domain of the primitive unit cell is defined by the actual system boundaries and these virtual boundaries. If the periodic boundary condition is set along the full two-dimensional translational vectors of the primitive unit cell (see the middle schematic in Fig. S2), we can obtain a series of energy dispersions as a function of the Bloch wavevectors. A mixed boundary condition that combines the pure-outgoing situation at infinity and the periodicity is possible as well (see the rightmost schematic in Fig. S2). This kind of boundary condition is necessary for computing the band structure in a one-dimensional photonic crystal satisfying the open boundary condition along one of the primitive unit cell directions while also satisfying the periodic boundary condition along another translational vector direction.

#### *Boundary shape of a single resonator quasi-atom*

The optical resonator quasi-atoms have two major system parameters: a refractive index inside the resonator and a boundary shape. The latter is controlled by a deformation parameter  $\varepsilon$  and is given as follows:

$$r(\theta; \varepsilon) = A(\varepsilon) [1 + \varepsilon \cos(t\theta + \theta_0)] , \quad \{\theta \in [0, 2\pi), t \in \mathbb{N}\}, \quad (\text{S15})$$

where  $A(\varepsilon)$  stands for the normalization constant,  $t$  is the periodicity of the resonator shape (e.g.,  $t = 3$  for  $C_3$  symmetry), and  $\theta_0$  the rotation of the resonator (see Fig. S3). It should be emphasized that although the results in our main text are discussed as if we focused only on the circular shape case (i.e.,  $\varepsilon = 0$ ), the overall band structures are robust against the deformation parameter  $\varepsilon$  (except for slight changes in the detailed structures caused by different resonator characteristics like area, perimeter length, curvature, etc.). More precisely, this robustness is observed in the Rayleigh scattering regime, in which the wavelength of the optical modes corresponding to low energy is larger than the resonator size ( $\sim \sqrt{\text{resonator area}}$ ). In this regime, the deformation effects are suppressed and ultimately negligible since the resonator area is smaller than that of the first Mie resonance. As we can see in Fig. S4, the global structure of the bands is not sensitive to the deformation parameter. Note that all energy bands in Fig. S4 are computed with the same refractive index as in Fig. 3(a),  $n = 4$ .

#### **Full characterization of the wave functions and parity eigenvalues at the TRIM points**

Figure S5–S7 present the full wave characters at the TRIM points in the BZ. By counting the parity eigenvalues of all the bands, we construct Table I, which summarizes the parity eigenvalue and the second Stiefel–Whitney number

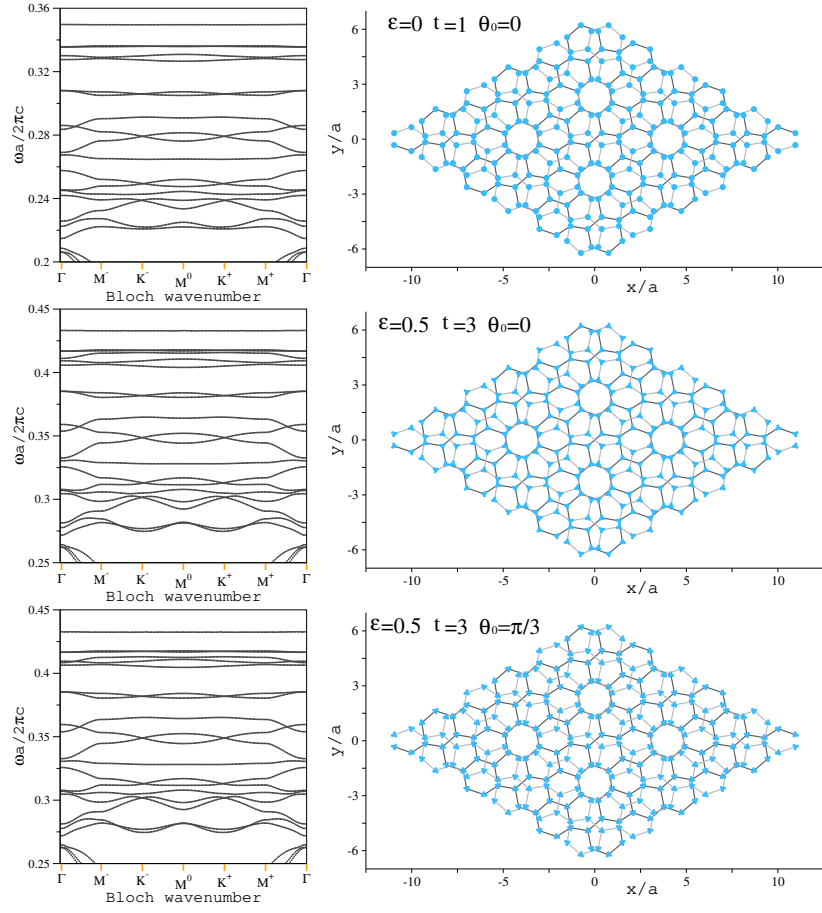


FIG. S4. Energy bands (left) of a twisted-bilayer hexagonal moiré superlattice (right) consisting of circular (top) and  $C_3$ -symmetric deformed (middle and bottom) quasi-atoms. The refractive index of the resonator quasi-atoms is  $n = 4$ . The deformed shape of the quasi-atoms is given by Eq. (S15).

of each band gap.

TABLE I. Parity classifications ( $\pm$ ) of the wavefunctions corresponding to the energy bands at the TRIM points,  $\{\Gamma, M^0, M^+, M^-\}$ , in the Brillouin zone.

Band	$\Gamma$	$M^\pm$	$M^0$	$M^+$	# of -	$\Sigma\# ; 4n + 0$ or $4n + 2$
1	+	-	+	-	2	2
2	+	+	-	+	1	3
3	-	-	-	-	4	7
4	-	+	+	+	1	8
5	+	+	-	+	1	9
6	-	+	-	+	2	11
7	+	-	+	-	2	13
8	+	-	+	-	2	15
9	+	+	-	+	1	16
10	+	-	+	-	2	18; $4 \times 4 + 2$ non-Triv.
11	-	+	-	+	2	20
12	-	-	+	-	3	23
13	-	+	-	+	2	25
14	-	-	+	-	3	28
15	-	-	+	-	3	31
16	-	+	-	+	2	33
17	-	-	+	-	3	36; $4 \times 9 + 0$ Trivial
18	+	+	-	+	1	37
19	+	-	+	-	2	39
20	-	+	-	+	2	41
21	+	+	-	+	1	42; $4 \times 10 + 2$ non-Triv.
22	+	-	+	-	2	44
23	+	-	+	-	2	46; $4 \times 11 + 2$ non-Triv.
24	+	-	-	-	3	49
25	-	+	+	+	1	50; $4 \times 12 + 2$ non-Triv.
26	-	+	-	+	2	52
27	-	+	-	+	2	54; $4 \times 13 + 2$ non-Triv.
28	+	-	+	-	2	56

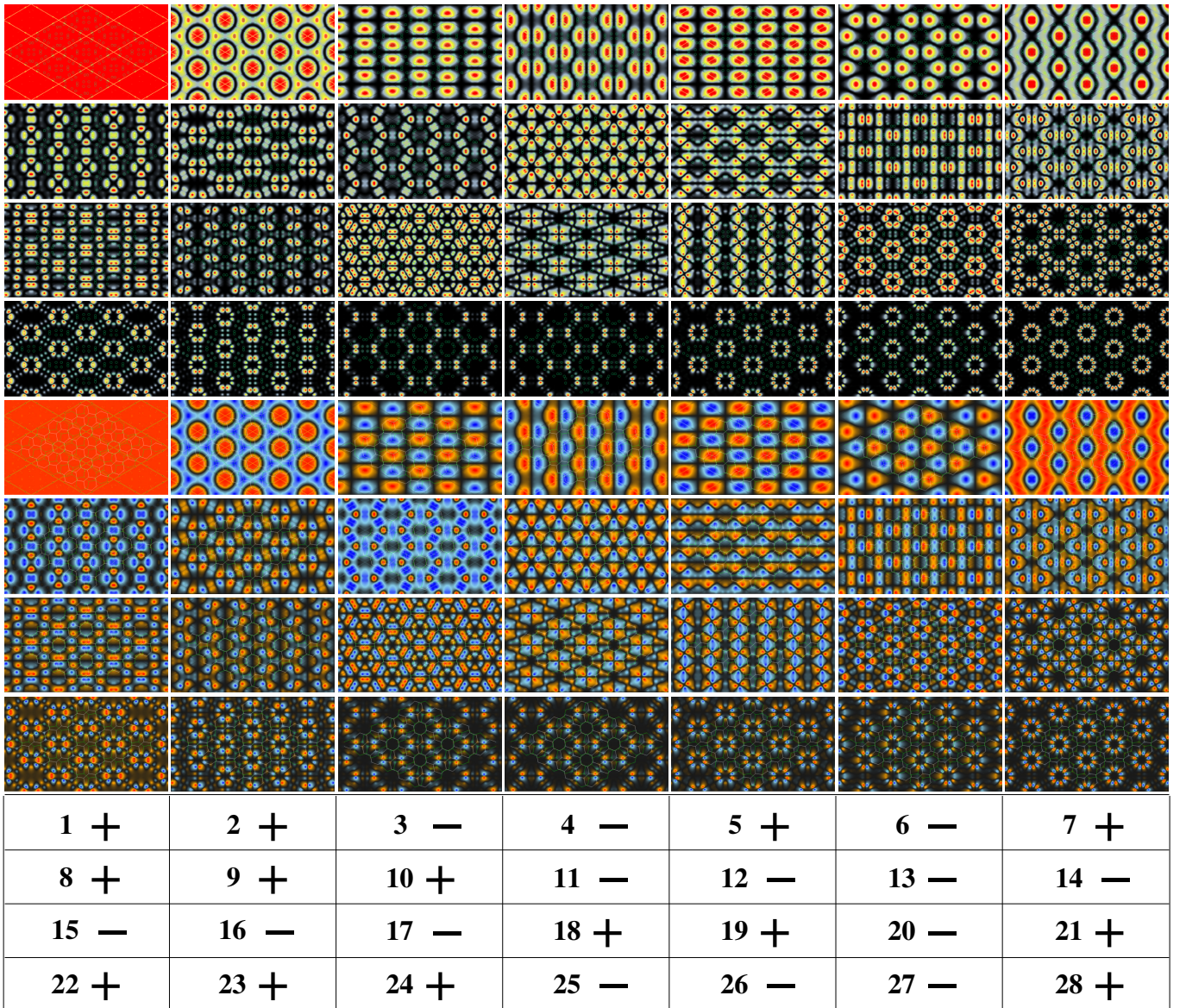


FIG. S5. Upper 4 rows: Wave intensities  $|\psi(\vec{r})|^2$  corresponding to the Bloch wavevector  $\Gamma$  and the energies  $\epsilon_j$  for bands  $j \in [1, 28]$ . Lower 4 rows: Real parts of the waves  $\text{Re}[\psi(\vec{r})]$  corresponding to the Bloch wavevector  $\Gamma$  and the energies  $\epsilon_j$  for bands  $j \in [1, 28]$ .

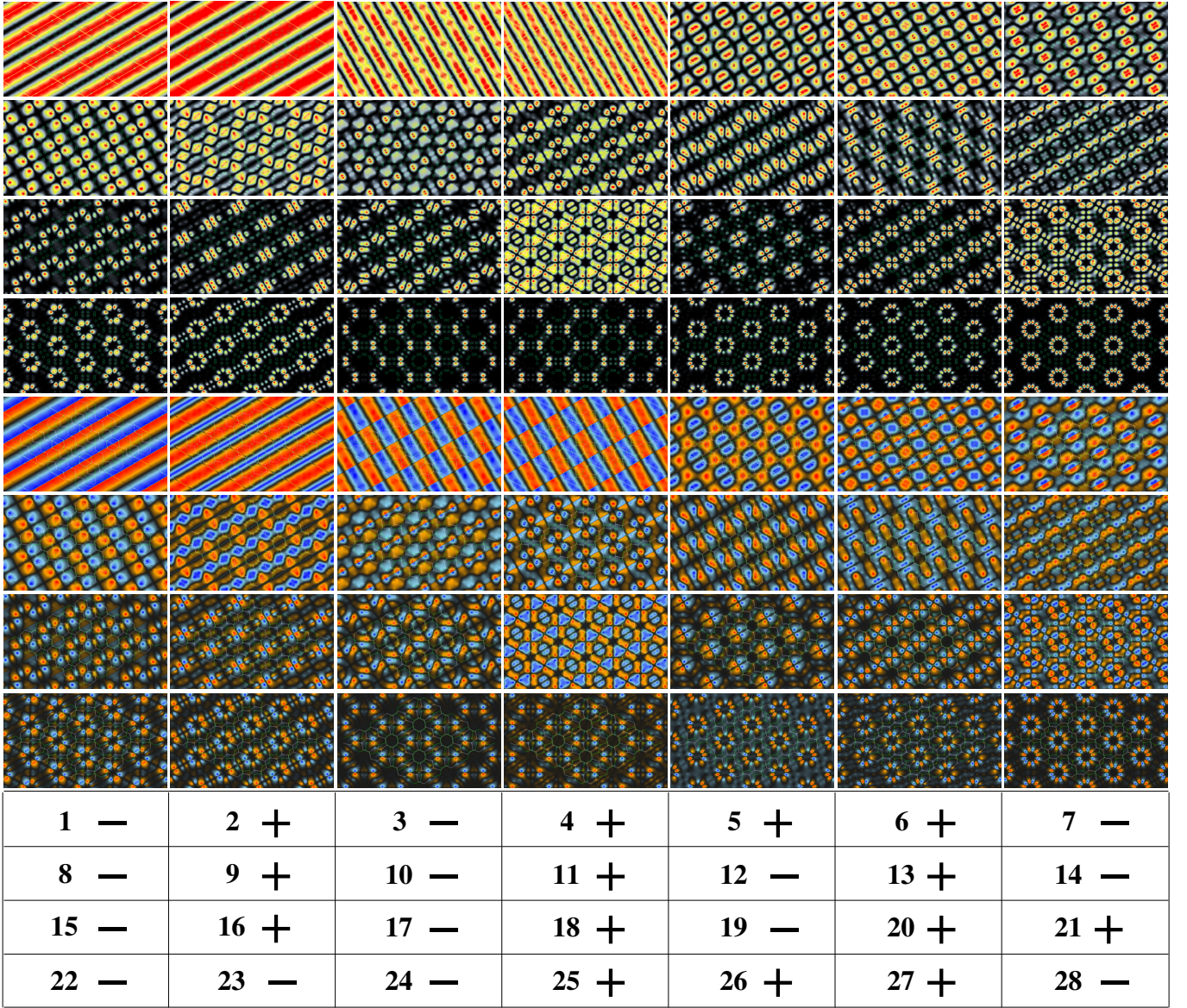


FIG. S6. Upper 4 rows: Wave intensities  $|\psi(\vec{r})|^2$  corresponding to the Bloch wavevector  $M^-$  and the energies  $\epsilon_j$  for bands  $j \in [1, 28]$ . Lower 4 rows: Real parts of the waves  $\text{Re}[\psi(\vec{r})]$  corresponding to the Bloch wavevector  $M^-$  and the energies  $\epsilon_j$  for bands  $j \in [1, 28]$ .

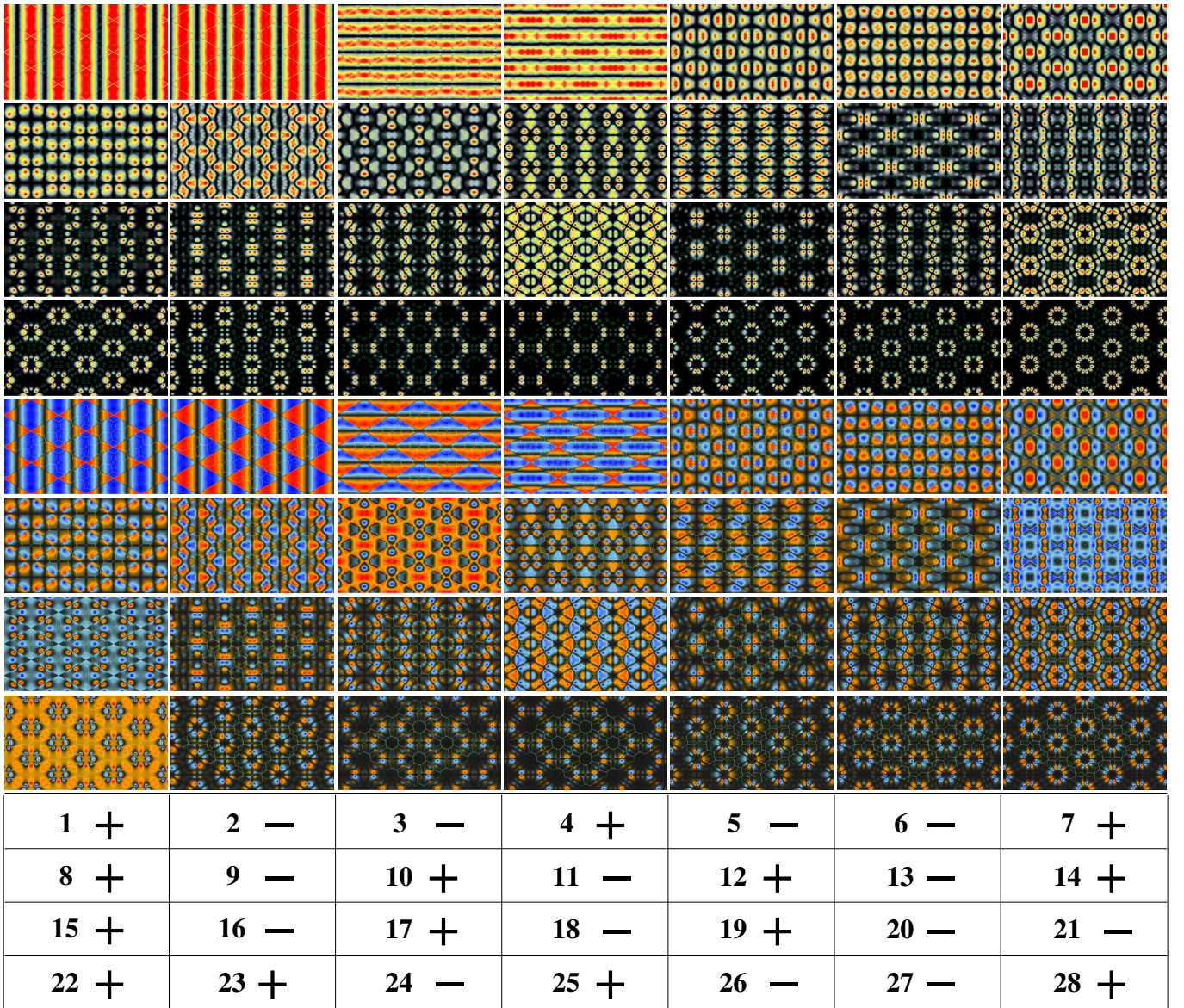


FIG. S7. Upper 4 rows: Wave intensities  $|\psi(\vec{r})|^2$  corresponding to the Bloch wavevector  $M^0$  and the energies  $\epsilon_j$  for bands  $j \in [1, 28]$ . Lower 4 rows: Real parts of the waves  $\text{Re}[\psi(\vec{r})]$  corresponding to the Bloch wavevector  $M^0 \Gamma$  and the energies  $\epsilon_j$  for bands  $j \in [1, 28]$ .